Remote Sensing of Environment 207 (2018) 71–83

Contents lists available at ScienceDirect

Remote Sensing of Environment

journal homepage: www.elsevier.com/locate/rse

Satellite estimation of coastal pCO_2 and air-sea flux of carbon dioxide in the northern Gulf of Mexico

Lohrenz S.E.[a,*], W.-J. Cai[b], S. Chakraborty[c], W.-J. Huang[d], X. Guo[e], R. He[f], Z. Xue[g], K. Fennel[h], S. Howden[i], H. Tian[j]

[a] School for Marine Science and Technology, University of Massachusetts Dartmouth, New Bedford, MA 02744, USA
[b] School of Marine Science and Policy, University of Delaware, Newark, DE 19716, USA
[c] School for Marine Science and Technology, University of Massachusetts Dartmouth, New Bedford, MA 02744, USA
[d] Department of Oceanography, National Sun Yat-sen University, Kaohsiung, Taiwan
[e] State Key Laboratory of Marine Environmental Science, Xiamen University, Xiamen, PR China
[f] Department of Marine, Earth, and Atmospheric Sciences, North Carolina State University, Raleigh, NC 27695, USA
[g] Department of Oceanography and Coastal Sciences, College of the Coast and Environment, Louisiana State University, Baton Rouge, LA 70803, USA
[h] Oceanography Department, Dalhousie University, Halifax, Nova Scotia, Canada
[i] School of Ocean Science and Technology, Division of Marine Science, University of Southern Mississippi, Stennis Space Center, MS 39529, USA
[j] School of Forestry and Wildlife Sciences, Auburn University, Auburn, AL, 36849, USA

ARTICLE INFO

Keywords:
Coastal ocean color
Coastal carbon cycling
Air-sea flux of CO_2
Gulf of Mexico
Mississippi River

ABSTRACT

Satellite approaches for estimation of the partial pressure of CO_2 (pCO_2) and air-sea flux of CO_2 in coastal regions offer the potential to reduce uncertainties in coastal carbon budgets and improve understanding of spatial and temporal patterns and the factors influencing them. We used satellite-derived products in combination with an extensive data set of ship-based observations to develop an unprecedented multi-year time-series of pCO_2 and air-sea flux of CO_2 in the northern Gulf of Mexico for the period 2006–2010. A regression tree algorithm was used to relate satellite-derived products for chlorophyll, sea surface temperature, and dissolved and detrital organic matter to ship observations of pCO_2. The resulting relationship had an r^2 of 0.827 and a prediction error of 31.7 µatm pCO_2 (root mean-squared error of the relationship was 28.8 µatm). Using a wind speed and gas exchange relationship along with satellite winds, estimates of air-sea flux of CO_2 were derived yielding an average annual flux over the period 2006–2010 of -0.8 to -1.5 (annual mean = -1.1 ± 0.3) mol C m^{-2} y^{-1}, where the negative value indicates net ocean uptake. The estimated total annual CO_2 flux for the study region was $-4.3 + 1.1$ Tg C y^{-1}. Relationships of satellite-derived pCO_2 with salinity were consistent with shipboard observations and exhibited a concave relationship with low values at mid- and low salinities attributed to strong biological drawdown of CO_2 in the high productivity river-mixing zone. The time-series of satellite-derived pCO_2 was characterized by a seasonal pattern with values lower during winter and spring, low to intermediate values during fall, and higher and more variable values during summer. These findings were similar to simulations from a coupled physical-biogeochemical model. A seasonal pattern was also evident in the air-sea flux of CO_2 with generally more negative fluxes (i.e., ocean uptake) during winter and spring, and positive fluxes during summer months with fall being a period of transition. Interannual variations in annual means of both air-sea flux of CO_2 and DIN loading were significant, with higher DIN loading coinciding in some cases with more negative air-sea flux of CO_2 (i.e., net ocean uptake). Spatial patterns of pCO_2 reflected regional environmental forcing including effects of river discharge, wind forcing, and shelf-slope circulation. Our study also illustrates the utility of satellite extrapolation for highlighting areas that may contribute significantly to regional signals and for guiding prioritization of locations for acquiring further observations. The approach should be readily applicable to other regions given adequate availability of in situ observations for algorithm development.

* Corresponding author.
E-mail addresses: slohrenz@umassd.edu (S.E. Lohrenz), wcai@udel.edu (W.-J. Cai), schakraborty@umassd.edu (S. Chakraborty), wjhuang29@mail.nsysu.edu.tw (W.-J. Huang), xhguo@xmu.edu.cn (X. Guo), rhe@ncsu.edu (R. He), zxue@lsu.edu (Z. Xue), katja.fennel@dal.ca (K. Fennel), Stephan.Howden@usm.edu (S. Howden), tianhan@auburn.edu (H. Tian).

https://doi.org/10.1016/j.rse.2017.12.039
Received 28 January 2017; Received in revised form 12 December 2017; Accepted 27 December 2017
Available online 03 February 2018

1. Introduction

Uncertainties in coastal carbon fluxes are such that the net uptake of carbon in the coastal margins remains a poorly constrained term in global budgets (Cai, 2011). The initial works of Borges et al. (2005), Cai et al. (2006) and Chen and Borges (2009) provided some of the first global assessments of sinks and sources of CO_2 in the coastal ocean, and highlighted the diversity and heterogeneity of coastal ecosystems and their associated carbon dynamics. Global estimates of coastal ocean CO_2 fluxes have continued to progress in the recent years, yet there remain significant inconsistencies in the recent global budgets for the estuarine CO_2 source and the continental shelf CO_2 sink (Bauer et al., 2013; Cai, 2011; Dai et al., 2013; Laruelle et al., 2010; Laruelle et al., 2014). None of these estimates fully resolves the seasonality or spatial heterogeneity in CO_2 fluxes and a major factor behind the uncertainties in these global budgets stems from the under sampling of the coastal oceans, or the continental margins (Dai et al., 2013; Gruber, 2015; Laruelle et al., 2015; Liu et al., 2010).

Satellite-based approaches for assessments of surface water partial pressure of CO_2 (pCO_2) distributions and air-sea fluxes of CO_2 are potentially powerful in their ability to provide broad spatial coverage and extended temporal coverage as well as a synoptic view that no field survey can match. Several satellite-based predictive models for estimating pCO_2 and the air-sea flux have been proposed recently. At present these algorithms use a variety of approaches ranging from the use of multivariate statistics (Chen et al., 2016; Chierici et al., 2012; Lohrenz and Cai, 2006; Shadwick et al., 2010; Signorini et al., 2013; Zhu et al., 2009) to machine-learning methods such as neural networks and self-organizing mapping techniques (Bai et al., 2015; Hales et al., 2012; Lefevre et al., 2002; Telszewski et al., 2009) and quasi-mechanistic reconstructions of pCO_2 based on the underlying total inorganic carbon and alkalinity changes in the context of known physical and biogeochemical processes (Bai et al., 2015; Hales et al., 2012).

Coastal ocean margins that receive input from large rivers represent extremes of continental shelf systems in carbon cycling and fluxes, and satellite observations can be particularly helpful in complementing ship-based observations and modeling approaches for characterizing carbon dynamics in these complex regions. Recent studies in the large river-dominated margins have highlighted the characteristics of these regions as sites of drawdown of surface water pCO_2 and net sinks for atmospheric CO_2. This appears to be a consequence of effects on pCO_2 of mixing of river and ocean water, as well as the action of a strong biological uptake stimulated by the input of river-borne nutrients. Examples of some of the large rivers dominating the different continental margins include the Amazon (Cooley et al., 2007; Kortzinger, 2003; Ternon et al., 2000) in the western tropical North Atlantic Ocean, Changjiang in the East China Sea (Bai et al., 2015; Shim et al., 2007; Tseng et al., 2014; Tsunogai et al., 1999; Zhai and Dai, 2009), Pearl in South China Sea (Cai et al., 2004; Guo et al., 2008; Guo et al., 2009), and the Mississippi-Atchafalaya river system (Cai, 2003; Cai and Lohrenz, 2010; Guo et al., 2012; Huang et al., 2015a) in the northern Gulf of Mexico, to name a few.

Here, we focus on the Mississippi and Atchafalaya River plume and surrounding coastal waters in the northern Gulf of Mexico. The Mississippi and Atchafalaya River System has been ranked as the seventh largest freshwater discharge system in the world (Milliman and Meade, 1983). Previous studies in this region have shown large cross-shelf gradients in pCO_2 with the inner shelf being a moderate seasonal sink (Cai, 2003; Huang et al., 2015a; Lohrenz and Cai, 2006; Lohrenz et al., 2010; Xue et al., 2016) despite high fluvial inputs of carbon (Ren et al., 2016; Ren et al., 2015; Tian et al., 2015). Modeling and ship-based observations also provide evidence for a distinct seasonal variation of air-sea CO_2 fluxes near the Mississippi River delta (Huang et al., 2015a; Lohrenz et al., 2010; Xue et al., 2016). Despite a growing body of work in this region, a recent synthesis of coastal ocean carbon fluxes in the region (Robbins et al., 2014) highlighted the need for additional data to adequately characterize seasonal and annual carbon fluxes in the Gulf of Mexico, as well as underlying spatial patterns. Over the last several years, we have conducted comprehensive field measurements of the carbon system properties (see Table 1 in Huang et al., 2015a) in the northern Gulf of Mexico. Yet, this dataset still gives an incomplete picture of the spatial and seasonal variability in CO_2 distributions and fluxes for the northern Gulf of Mexico. Recent modeling approaches have provided an independent assessment, validated by in situ observations, of the dynamics of carbon in the northern Gulf and the associated seasonal patterns (Xue et al., 2016). Here, we provide another independent analysis of seasonal and spatial patterns in both pCO_2 and air-sea flux of CO_2 based on satellite imagery and compare our results to the in situ observations and modeled findings. Our objectives were: i) to provide an assessment of satellite-based approaches for characterizing the spatial and temporal variability of the surface ocean pCO_2 and sea-air CO_2 flux for the northern Gulf of Mexico, and ii) to investigate the seasonal CO_2 dynamics across the continental margin and elucidate the interannual variations and possible environmental drivers.

Table 1
Model results for different variable combinations (PE = prediction error in µatm, MB = mean bias in µatm, MR = mean ratio, unitless).

Variable combinations	PE	r^2	MB	MR
chlor_a, Kd_531_lee, sat_sst	30.8	0.832	1.411	1.010
chlor_a, adg_443_gsm, sat_sst	31.7	0.827	− 0.526	1.004
chlor_a, adg_443_qaa, sat_sst	38.6	0.806	− 0.894	1.004
nflh, adg_443_gsm, sat_sst	32.6	0.827	− 0.726	1.002
nflh, Kd_531_lee, sat_sst	34.6	0.790	− 0.569	1.004

2. Materials and methods

2.1. Field observations

Data for this study were obtained during a series of cruises conducted in the northern Gulf of Mexico (Fig. 1) from 2006 to 2010. These included four cruises on the U.S. Environmental Protection Agency Ocean Survey Vessel *Bold* during 6–11 June 2006, 6–11 September 2006, 2–8 May 2007, and 18–24 August 2007, focusing largely on the area of recurrent hypoxia in the northern Gulf of Mexico (Guo et al., 2012). Additional shelf-wide cruises were conducted on the R/V *Cape Hatteras* 8–20 January 2009, 19 April–1 May 2009, 18–30 July 2009, and 10–22 March 2010 and on the R/V *Hugh G. Sharp* 28 October–9 November 2009. These cruises were selected because they covered a large portion of the study area encompassing inner to outer shelf water mass regimes and were representative of different seasonal and river discharge conditions. Underway determinations of sea surface pCO_2 were made by directing flow from the ship's flow-through to a shower head equilibrator plus infrared detector system as previously described (Huang et al., 2015a; Pierrot et al., 2009). Ship-based observations of sea surface salinity (SSS) and temperature (SST) were measured using a Seabird SBE-45 flow-through thermosalinograph.

2.2. Satellite ocean color estimation of pCO_2

Previously, we have used principal component analysis and multiple regressions (Lohrenz and Cai, 2006; Lohrenz et al., 2010) to develop empirical relationships between surface ocean pCO_2 and SST, salinity, and chlorophyll. We then used satellite-retrieved Moderate Resolution Imaging Spectroradiometer (MODIS) Aqua products as proxies of these variables to estimate the regional distributions of pCO_2. However, to apply this approach to satellite data requires the intermediate step of retrieving satellite estimates of the predictor variables, SST, salinity and chlorophyll, and using these retrieved estimates in the empirical algorithm. This approach has the potential to introduce additional uncertainty associated with the uncertainties in the retrieved products.

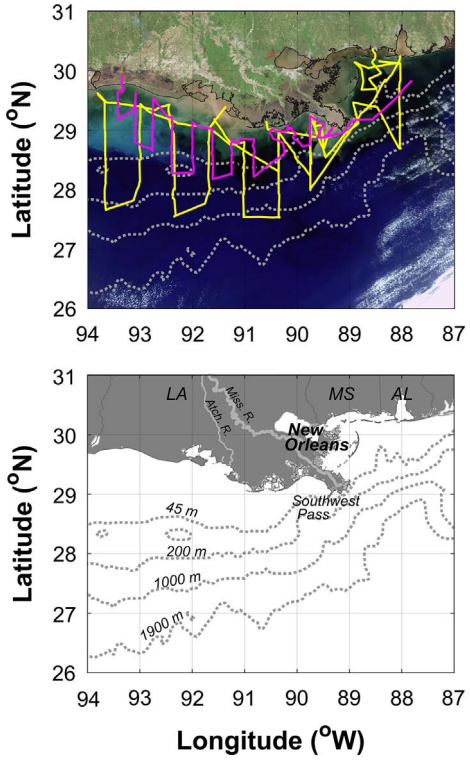

Fig. 1. The study region in the northern Gulf of Mexico illustrating the bathymetry (upper panel) and representative cruise tracks for the 2006–2007 (magenta line) and 2009–2010 (yellow line) cruises overlaid on a true color MODIS Aqua image from 14 April 2009.

Here, we used regression tree analysis to directly relate surface ocean pCO_2 to satellite-retrieved products, thus avoiding the intermediate step. The regression tree is a machine-learning algorithm that splits the data into multiple groups based on rank ordering so as to maximize homogeneity of the resulting groups (De'ath and Fabricius, 2000).

Image data were acquired from the NASA Ocean Biology Distributed Active Archive Center (OB.DAAC) at Goddard Space Flight Center. Level 0 files were processed to quasi-250 m resolution Level 2 products using the SeaDAS data analysis system version 7.3.3 (Baith et al., 2001). Products included chlorophyll *a* (chlor_a), normalized fluorescence line height (nflh), detrital and dissolved absorption at 443 nm (adg_443_gsm or adg_443_qaa), diffuse attenuation coefficient at 531 nm (Kd_531_lee), and sea surface temperature (sat_sst). The chlor_a product as implemented in SeaDAS uses a combination of the standard band ratio algorithm for MODIS (OC3M) and the Hu et al. (2012) Color Index (CI) chlorophyll *a* algorithm. The SeaDAS algorithm differs from Hu et al. (2012) in that the transition between CI and OC3M occurs for the range $0.15 <$ CI-derived chlorophyll < 0.2 mg m^{-3}. The nflh product is a chlorophyll fluorescence index derived as the difference between normalized water leaving radiance at 678 nm and the interpolated baseline between the two adjacent wavebands (Behrenfeld et al., 2009). The adg_443_gsm product was derived using the Garver-Siegel-Maritorena semi-analytical algorithm (Maritorena et al., 2002) and the adg_443_qaa product was derived using the Lee et al. (2002) quasi-analytical algorithm (version 6). The Kd_531_lee product was derived using the Lee et al. (2005) algorithm. To ensure a high degree of quality, pixels were excluded if they were associated with the following quality control flags as per Chen et al. (2016): atmospheric correction failure, land, sun glint, high radiance, large sensor viewing angle ($> 60°$), stray light, cloud/ice, high solar zenith angle, low water-leaving radiance (low nLw_555), questionable navigation, chlor_a > 64 or < 0.01 mg m^{-3}, suspicious atmospheric correction, dark pixel (scan line error) and navigation failure. Minimum allowable quality level for sat_sst was set to 1 (zero being the highest quality and 2 being the default setting).

Matchups between satellite observations and ship-based underway measurements of pCO_2 were retrieved for 3×3 pixel windows co-located with observations made within $\pm$ 6 h of image acquisition. Level 2 products were retrieved from these files for the locations corresponding to the underway pCO_2 survey. Values of $pCO_2 > 1200$ µatm were excluded as these corresponded to a very limited set of data within or near the mouth of the Mississippi River. Data ranges for the training dataset were 0.0087–4.94 m^{-1} (adg_443_gsm), 0.052–1.81 m^{-1} (Kd_531_lee), 11.7–31.8 °C (sat_sst), 0.040–51.1 mg m^{-3} (chlor_a), and nflh (0.0011–3.97). For those variables for which ship-based measurements acquired within $\pm$ 6 h of the satellite overpass were available, we found reasonable agreement with the satellite-derived products for the corresponding 3×3 pixel array centered at the sampling location (Fig. S1). The regression tree function in MATLAB® vR2016b software (fitrtree) was applied to develop the empirical relationship between ship-based pCO_2 observations and the satellite products (chlor_a or nflh, adg_443_gsm or adg_443_qaa or Kd_531_lee, and sat_sst). With the exception of sat_sst, the data were natural log-transformed to normalize their distributions prior to use in the analysis. A bootstrap approach was used whereby the data were randomly subsampled such that half the data were used as a "training" dataset to derive the algorithm and the other half used to evaluate algorithm performance by comparing the estimated values of pCO_2 for the test dataset to the corresponding observed values. A "deep" regression tree was developed to account for the complexity of the large dataset. The minimum "parent size" or smallest size for the number of branch node observations was 5. To reduce "overfitting", the resulting regression tree was "pruned" using the "prune" MATLAB® function to produce a less complex tree without substantially compromising performance. To evaluate model uncertainty, a cross-validation approach was used by randomly dividing the training data into ten subsets and training ten new trees, each one on nine parts of the data. The predictive accuracy of each new tree on the data not included in the training set was then examined to determine the prediction error (PE). The lowest PE and highest r^2 were achieved using the combination of chlor_a, Kd_531_lee, and sat_sst (Table 1). Comparable performance was achieved using the adg_443_gsm product instead of the Kd_531_lee product. Other variable combinations that were evaluated exhibited lower r^2 and higher prediction errors (Table 1). We chose to use the chlor_a, adg_443_gsm, and sat_sst product combination in all subsequent analyses as these variables had clear relationships to either distinct biogeochemical constituents in the case of chlor_a and adg_443_gsm or a key physical property in the case of sat_sst (Fig. S1). A detailed listing of the regression tree source code along with a copy of the MATLAB® tree file is given in supplementary material (Table S1). Information about the variable means and ranges for each region for the matchup dataset used to develop the model is given in Table S2.

Regarding the issue of collinearity (correlations among input variables), the ln(chlor_a) and ln(adg_443_gsm) variables were correlated ($r > 0.9$). Because the regression tree segments the data into smaller subsets and because we are limiting the use of the algorithm to a geographic region and environmental range for which the algorithm was trained, correlations among variables should be less of a concern (e.g., Dormann et al., 2013). However, to further examine effects of collinearity, we conducted a separate analysis using orthogonal component variables derived from principal component analysis (PCA) of the input variables. We also examined the performance of the algorithm trained using standard resolution (1.1 km) rather than the quasi-250 m resolution satellite products (see comparisons in Results).

The regression tree algorithm was applied to daily imagery for each cruise to derive estimates of pCO_2 and results were compared to the ship-based observations. Images of satellite products (chlor_a, adg_443_gsm, sat_sst) were generated by processing the daily L0 MODIS Aqua imagery through Level 2 (L2) to the 1.1 km resolution Level 3 (L3) daily products. Because performance of the algorithm was unstable for input data falling outside the range of the training dataset, we held

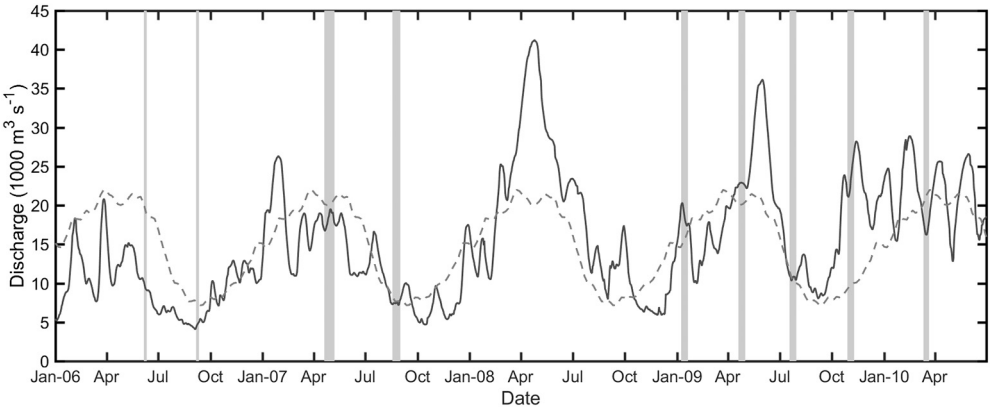

Fig. 2. Mississippi River discharge during the study period. The dark solid line is the daily river discharge as determined at the Tarbert Landing, MS discharge site (Gage ID 01100) located at approximately river mile 306.3. The dashed line represents the 5-day average over the period from 1995 to 2010. The vertical gray bars indicate cruise periods. Discharge data provided courtesy of the Army Corps of Engineers.

values of adg_443_gsm (hereafter adg_443) and chlor_a to minimums of 0.05 m^{-1} and 0.04 mg m^{-3}, respectively. Maximum values of sat_sst were held to 32 °C. Values of adg_443 > 5 m^{-1}, chlor_a > 50 mg m^{-3}, and sat_sst < 11 °C were omitted from the analysis. Highest algorithm-derived values of pCO_2 were capped at 600 µatm as this encompassed the majority of ship-based observations (Fig. S2). This also eliminated instances at a small number of locations for which the regression tree improperly assigned anomalously high values of pCO_2, which could have a disproportionate impact on computed fluxes. We found that it was nevertheless necessary to retain values of pCO_2 up to 1200 µatm in the training dataset to ensure that the upper range of the ship-based observations were properly represented in the satellite-derived results. Values of ship-based observations of pCO_2 were compared to the mean pCO_2 value of the image for the corresponding 3 × 3 pixel array centered at the location of the ship-based sample acquired within ± 6 h of the satellite overpass. Data were binned by salinity in unit increments of 2 for comparison.

A time-series of pCO_2 imagery was developed by generating products for the period from 2006 to 2010 and applying the satellite empirical algorithm to derive pCO_2. The daily L1A MODIS Aqua imagery were processed through L2 to L3 products for chlor_a, adg_443, and sat_sst at 1.1 km nominal resolution, and the pCO_2 algorithm was applied to the L3 mapped products. The daily pCO_2 products were averaged over 8-day intervals to generate a time-series. Comparisons were made for means for inner shelf (< 45 m), shelf (< 200 m), and open Gulf waters to independent data for the same regions and time periods from the Surface Ocean Carbon Atlas (SOCAT) (Bakker et al., 2016), excluding that associated with the training dataset. We also compared the satellite time-series to modeled simulations of pCO_2 from Xue et al. (2016).

2.3. Air-sea flux of carbon dioxide

Satellite-derived regional assessments of sea surface pCO_2 were used in conjunction with estimates of wind fields and atmospheric pCO_2 to produce regional-scale estimates of air-sea fluxes. Following convention (Huang et al., 2015a), air-sea flux of carbon dioxide, F_{CO_2}, can be estimated as:

$$F_{CO_2} = k \; K_0 \; [pCO_{2(sw)} - pCO_{2(air)}] \quad (1)$$

where k (cm h^{-1}) is the gas transfer velocity (piston velocity) of CO_2, K_0 (mol L^{-1} atm^{-1}) is the solubility coefficient of CO_2 at the in situ temperature and salinity (Weiss, 1974), and $pCO_{2(sw)}$ and $pCO_{2(air)}$ (µatm) are the water-saturated partial pressures of CO_2 in seawater and air, respectively. Satellite estimates of salinity were made using an empirical relationship between adg_443 and salinity (Fig. S3). Positive values of F_{CO2} indicate a transfer of CO_2 from the water to the atmosphere. For flux calculations, an air mole fraction of CO_2 (xCO_2) for the entire Gulf of Mexico was estimated from observations acquired by the Atmospheric Infrared Sounder (AIRS) following the procedures described in Xue et al. (2016). Values of $pCO_{2(air)}$ were then determined as follows:

$$pCO_{2(air)} = xCO_{2(air)}[P_{baro} - P_{sw}], \quad (2)$$

where P_{baro} is the climatological monthly mean barometric pressure at sea surface from the NCEP Reanalysis data (NCEP Reanalysis Data, 2017) and P_{sw} is the surface seawater vapor pressure at sea surface temperature and salinity (Weiss and Price, 1980). The gas transfer velocities were estimated for each 8-day period following the method of Wanninkhof (2014). Satellite wind data (Cross-Calibrated Multi-Platform Ocean Surface Wind Vector L3.0 6 h, 0.25° resolution) were acquired from the NASA Physical Oceanography Distributed Active Archive (Atlas et al., 2011) and were interpolated to the resolution of the L3 imagery to derive gas transfer velocities for air-sea flux calculations. Representative vector maps of satellite-derived wind speed during each cruise are given in Fig. S4.

3. Results

3.1. River discharge patterns

River discharge data (Fig. 2) were acquired from the U.S. Army Corps of Engineers for the Tarbert Landing discharge site (Gage ID 01100) located at approximately river mile 306.3. This site was chosen as it is located below the Old River Control structure, which diverts water to the Atchafalaya River such that of the flow coming from the entire Mississippi-Atchafalaya basin, the fractions of discharge for the Mississippi and Atchafalaya rivers are 70% and 30% respectively (Goolsby et al., 1999). As there are no other major locks or dams on the river below Tarbert Landing, the discharge at this site is considered to be representative of that exiting through the Belize (or bird-foot) delta (Fig. 2). Additional discharge data for the Atchafalaya River were obtained from the Simmesport (Gage ID 03045) station (river mile 4.9). Maximum discharge generally occurs during the late winter or spring. Compared to the 16 year (1995–2010) annual average discharge (14.7 × 10^3 m^3 s^{-1}), 2006 was a below average flow year (9.78), 2007 was close to the average (12.9), and 2008–2010 (18.2, 18.3, 16.2) were above average flow years.

3.2. Satellite-derived estimation of pCO_2

The regression tree algorithm for estimation of pCO_2 from satellite observations had a resubstitution error of 9.6 µatm and a prediction error (PE) of 31.7 µatm. The resubstitution error was the difference between the response training data (i.e., the observed value of pCO_2 for the input data) and the prediction the tree makes for the corresponding input data. The PE is that determined by the cross-validation approach described previously and represents the error associated with estimates

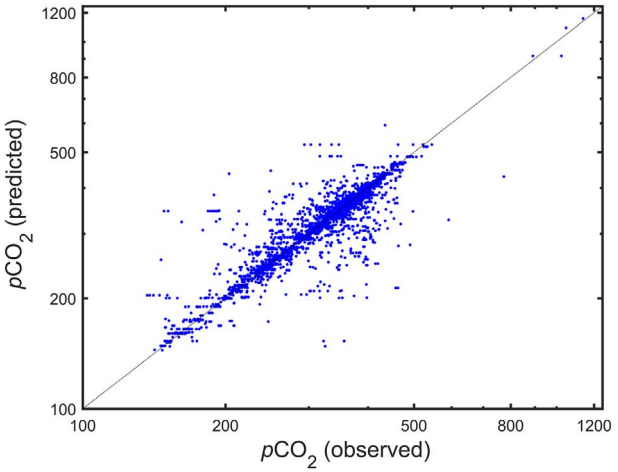

Fig. 3. Estimates of pCO_2 (μatm) from the regression tree empirical algorithm resulted in strong correlations between observed and predicted pCO_2. Value of the adjusted r^2 for the relationship was 0.827 (N = 5149). The prediction error for the regression tree was 31.7 μatm. Substitution error was 9.6 μatm. The black line represents the 1:1 relationship.

Table 2
Model results for selective omission of input variables (abbreviations as in Table 1).

Variable omitted	PE	r^2	MB	MR
None	31.7	0.827	− 0.526	1.004
chlor_a	36.7	0.784	− 1.212	1.003
adg_443_gsm	37.9	0.748	0.006	1.008
sat_sst	56.1	0.473	0.852	1.020

of pCO_2 for new data (data not used in training). A further evaluation of algorithm performance was made by comparing the pCO_2 estimated from the satellite products using the regression tree algorithm with the test dataset (i.e., the data randomly selected and excluded from training set) with the observed pCO_2. This relationship (Fig. 3) yielded an adjusted r^2 of 0.827, a root mean squared error (RMSE) of 28.8 μatm, and a mean absolute error (MABE) of 12.3 μatm. The mean bias (MB) for this relationship was − 0.526 μatm and mean ratio (MR) was 1.004, an outcome that demonstrates that the regression tree approach resulted in relatively low systematic bias. Omission of any one of the input variables resulted in a lower r^2 and higher PE (Table 2) with the largest effect due to omission of sat_sst. Effects on r^2 and PE due to omission of either chlor_a or adg_443_gsm resulted in a similar degradation in performance.

Algorithm stability was evaluated by introducing random variability to each of the input variables comparable to expected uncertainties in the satellite products, using a + 20% range in either chlor_a or adg_443, or a + 1 °C difference in sat_sst (Table 3). The model appeared to be most sensitive to variability in sat_sst, which resulted in the highest PE (46.8 μatm). Introducing variability in either chlor_a or adg_443_gsm resulted in a slightly lower r^2 and higher PE, but to a lesser degree than was seen for sat_sst.

The regression tree algorithm was applied to composite MODIS Aqua L3 imagery to generate monthly maps of pCO_2 corresponding to each cruise period (Fig. 4). The pCO_2 images were characterized by predominantly lower values in the shelf region and higher values offshore. Low values of pCO_2 were especially evident during spring as exemplified by the May 2007 and March 2010 images (Fig. 4). Values in offshore waters were higher particularly during summer months, presumably related to temperature effects on solubility. Monthly composite images of chlor_a (Fig. S5), adg_443_gsm (Fig. S6), and sat_sst (Fig. S7) were provided for comparison in supplementary material. High values of chlor_a extending offshore can be seen in the Mar 2010 composite (Fig. S5) and relatively high temperatures in August 2007 and July 2009 (Fig. S7).

Table 3
Model sensitivity to random variation in input variables (abbreviations as in Table 1).

Variable	Effect	PE	r^2	MB	MR
None	N/A	31.7	0.827	− 0.526	1.004
chlor_a	± 20%	36.5	0.777	0.134	1.007
adg_443_gsm	± 20%	39.8	0.764	0.739	1.008
sat_sst	± 1 °C	46.8	0.708	− 0.294	1.007

Match-ups between satellite and in situ pCO_2 binned by salinity range showed general consistency in observed versus satellite-derived values (Fig. 5). The pattern of variation in pCO_2 was characterized by values close to atmospheric levels at high salinities, lower values in the mid-salinity regions, and increases at low salinities. While the trends in satellite-derived and ship-based observations of pCO_2 were generally consistent, there were some differences, particularly at lower salinities. We noted that the algorithm also tended to underestimate pCO_2 at very high salinities for the September 2006 and July 2009 datasets (Fig. 5). Despite these differences, the satellite-derived pCO_2 exhibited trends that were generally consistent with the ship-based measurements.

A seasonal cycle was evident in the 8-day composite time-series of pCO_2 (Fig. 6), characterized by higher values in summer months and lower during spring and winter. Low or intermediate values of pCO_2 were observed during fall. Values of pCO_2 for open Gulf waters ranged from a high of 426 μatm in August 2010 to 342 μatm in January 2010. The amplitudes of the seasonal variations were larger for the shelf (< 200 m) and inner shelf (< 45 m) regions. For shelf waters, the highest pCO_2 was observed during July 2006 (504 μatm) and lowest values (271 μatm) in March 2010. The highest pCO_2 for inner shelf waters (530 μatm) was also during July 2006 and lowest values (252 μatm) in March 2010. Levels of pCO_2 were below atmospheric levels during much of the year with the exception of summer months when surface water pCO_2 values exceeded atmospheric levels. Satellite-estimated pCO_2 exhibited similar patterns in temporal variation to that of the ship-based observations, including observations not used in the development of the algorithm that were acquired through the SOCAT database. The seasonal temporal pattern in the satellite times-series also tracked that of the modeled pCO_2 time series from Xue et al. (2016). However, the model simulations were characterized by a larger seasonal amplitude particularly for shelf waters. The model-simulated pCO_2 tended towards higher values in late spring, summer, and early fall. Satellite estimated pCO_2 also tended to exhibit more short-term variability, particularly evident as episodic peaks during summer months.

Results for pCO_2 output for the PCA approach were evaluated for comparison. The PCA-modified version of the algorithm had a similar r^2 of 0.826, but a slightly higher prediction error of 35.3 μatm pCO_2. The PCA approach underestimated in some instances the average pCO_2 values for shelf and inner shelf waters (cf. Figs. 6 and S8). Therefore, we chose not to use PCA given that it did not substantially improve the performance of the algorithm. Similarly, we also compared the algorithm trained using the 1.1 km resolution satellite products. Although the resulting regression tree had a relatively high r^2 (0.941) and low prediction error (22.3 μatm), it did not perform as well in representing the full extent of temporal variability in signals (cf. Fig. 6 and Fig. S9) and was therefore not used (see Discussion).

3.3. Air-sea flux of CO_2

The pattern of seasonal variation in air-sea flux of CO_2 (Fig. 7) paralleled that of pCO_2 with more negative (net ocean uptake) fluxes during winter and spring, positive (net ocean emission) fluxes in summer months, and with fall being a period of transition (Table 4). Values of air-sea flux of CO_2 for open Gulf (> 200 m) waters ranged from a positive (sea-to-air) flux of 3.1 mmol C m^{-2} d^{-1} in Jul 2006 to a

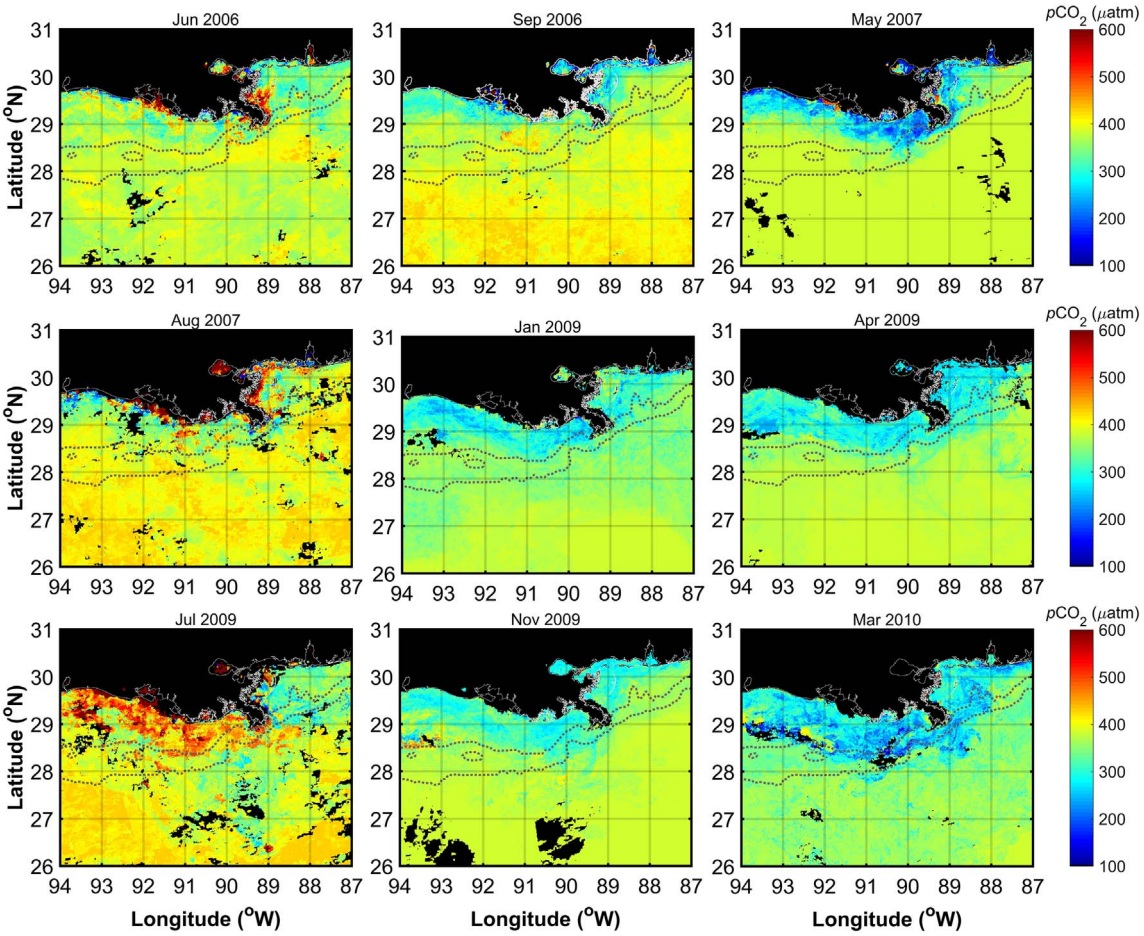

Fig. 4. Monthly composite Images of satellite-derived pCO_2 corresponding to each of the cruises for which observational data were acquired. Black pixels in the images correspond to areas that were masked (e.g., land, clouds), as described in Methods. The dotted lines represent the 45 and 200 m isobaths.

negative of -9.7 mmol C m^{-2} d^{-1} in Mar 2010. As in the case of pCO_2, the amplitudes of the seasonal variations were larger for the shelf (< 200 m) region. For shelf waters, the highest positive flux was observed during Jul 2006 (10.4 mmol C m^{-2} d^{-1}) and lowest negative flux (-30.6 mmol C m^{-2} d^{-1}) in Mar 2010. Inner shelf (< 45 m) fluxes were generally more negative that outer shelf (45–200 m) fluxes (Table 4). The satellite-derived estimates of air-sea CO_2 flux were generally in good agreement with the ship-based estimates by Huang et al. (2015a) (circle symbols in Fig. 7).

The seasonal pattern of air-sea flux of CO_2 was out of phase with both the combined river discharge and dissolved inorganic nitrogen (DIN) loading from the Mississippi and Atchafalaya rivers (bottom panel in Fig. 7). River discharge and DIN loading generally peaked in spring, prior to the summer period of positive net sea to air flux of CO_2 (Fig. 7). The peak value of DIN loading (4.18×10^6 kg N d^{-1}) occurred in both Apr 2008 and May 2009, while the lowest (0.254×10^6 kg N d^{-1}) was observed in Aug 2006. The peak fluxes in DIN coincided with maxima in river discharge during those years (Fig. 7).

We sought to examine whether there were relationships between DIN loading and river discharge with other variables on seasonal time scales. Cross-correlation analyses did reveal significant positive correlations in the relationship of DIN loading and river discharge to satellite chlor_a, adg_443, sat_sst, pCO_2, and CO_2 flux (Table 5); highest correlations were observed for time lags between the satellite-derived time-series and either DIN loading or river discharge of 0 to 120 days (Table 5). Shelf and inner shelf chlor_a and adg_443 generally exhibited small positive lags (0 to 24 days) relative to river inputs. Lags relative to shelf pCO_2 and CO_2 flux were longer, ranging from 72 to 120 days. Relatively long lags were also observed in the relationship of sat_sst to DIN loading and river discharge (96 to 120 days). Open Gulf chlor_a also exhibited relatively long lags in relationship to DIN loading (112 days), but a zero lag relative to river discharge.

Average annual fluxes of CO_2 (Table 6) differed significantly among the different regions based on one-way analysis of variance (ANOVA: $F_{(2,687)} = 67.5$, $p < 0.0001$). Post hoc comparisons using the Tukey HSD test indicated that fluxes were progressively more negative (greater uptake by seawater) going from open Gulf to shelf to inner shelf (Table S3). Significant interannual variations of CO_2 fluxes within regions were also evident, as supported by ANOVA (open Gulf: $F_{(4,225)} = 4.36$, $p = 0.0021$; shelf: $F_{(4,225)} = 3.08$, $p = 0.017$; inner shelf: $F_{(4,225)} = 2.84$, $p = 0.025$; total: $F_{(4,225)} = 3.53$, $p = 0.0081$). For open Gulf waters, post hoc comparisons using the Tukey HSD test indicated that fluxes during 2010 were more negative than observed in both 2006 and 2007 (Table S4). For shelf and inner shelf waters, fluxes during 2008 were more negative than during 2007, and for the combined total fluxes for the entire study region, fluxes during both 2008 and 2010 were more negative than during 2007 (Table S4). Annual average DIN loadings (Table 6) also differed between years (ANOVA: $F_{(4,225)} = 7.57$, $p < 0.00001$), with significantly lower loading in 2006 as compared to 2008, 2009 and 2010 (Table S5).

Consistent with the findings that annual CO_2 fluxes were more negative and DIN loading higher during 2010, we noted previously that the largest magnitude negative CO_2 flux was in March 2010 (indicated by arrow in Fig. 7). A large expanse of relatively low pCO_2 over the shelf was also evident in the imagery for that month (Fig. 4). The March 2010 period was preceded by an unusually high period of discharge

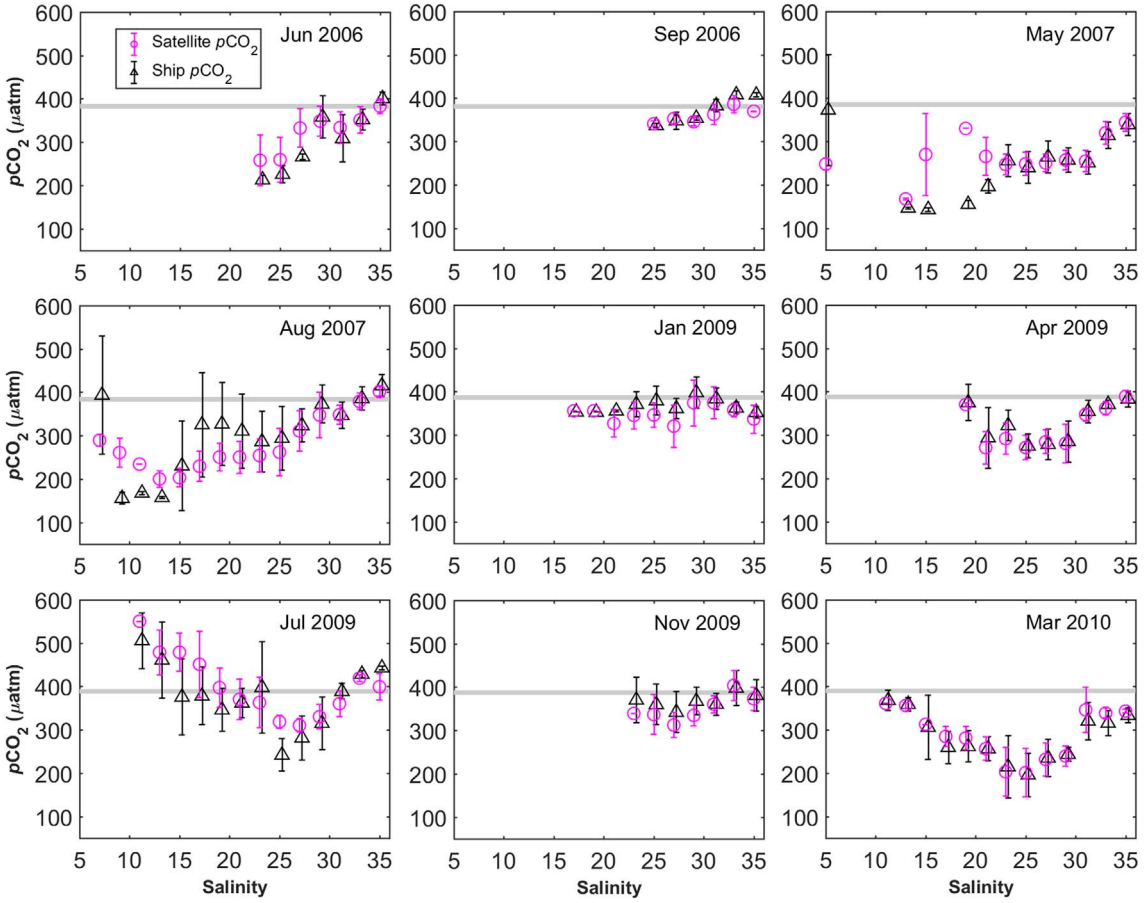

Fig. 5. Comparison between satellite-derived pCO_2 (open circles) and ship-based observations (triangles) along the salinity gradient for the different cruise periods. Salinity data were those acquired from the underway measurements and were binned over increments of two salinity units. The horizontal gray line represents the atmospheric pCO_2 value. Symbol error bars are plus or minus one standard deviation of the mean for each salinity bin.

(Fig. 2) and DIN loading (Fig. 7). Prior studies have documented the widespread nature of the river plume during that time frame (Huang et al., 2013).

Total annual CO_2 fluxes for the study area (Fig. 1) were derived for each of the subregions (Table 7), including open Gulf (> 200 m), shelf (< 200 m), inner shelf (< 45 m) and outer shelf (45–200 m). The estimated areas of the subregions are given in Table S6. Total annual Gulf CO_2 fluxes ranged from −1.0 to −2.3 Tg C y^{-1}, while shelf fluxes ranged −2.0 to −3.6 Tg C y^{-1}. Inner shelf fluxes accounted for the majority of the total annual shelf CO_2 flux, and in most years accounted for more than half of the total CO_2 flux for the region. The overall mean total annual flux for the region and period of study was −4.3 ± 1.1 Tg C y^{-1}.

3.4. Uncertainties in air-sea flux of CO_2

The errors presented thus far such as in Tables 4 and 6 correspond to the variance associated with region and temporal mean values. Uncertainties in air-sea fluxes at a given location and time can be estimated through systematic assessment of sources of error in the terms used in Eq. (1) to compute the fluxes. Uncertainty in the coefficient of gas transfer, k, was assumed to be 20% as given in Wanninkhof (2014). Uncertainty in the solubility coefficient, K_o, for the expected uncertainties in satellite-derived sea surface temperatures (± 1 °C) and salinity (± 5) were determined to be < 4%. The other sources of uncertainty are due to the air and seawater estimates of pCO_2. We assumed an air pCO_2 uncertainty of 6 µatm, following the precedent of Huang et al. (2015a). For seawater pCO_2, we used the PE of 31.7 µatm as estimated for the full regression tree algorithm. Through propagation of errors, we estimate the relative uncertainty in air-sea flux to be the following:

$$\partial F_{CO_2} = F_{CO_2}\sqrt{\left(\frac{\partial k}{k}\right)^2 + \left(\frac{\partial K_o}{K_o}\right)^2 + \left(\frac{\partial \Delta pCO_2}{\Delta pCO_2}\right)^2}, \quad (2)$$

where $\frac{\partial k}{k}$ is the fractional uncertainty in the coefficient of gas transfer (0.2), $\frac{\partial K_o}{K_o}$ is the fractional uncertain in the solubility coefficient (0.04), and $\frac{\partial \Delta pCO_2}{\Delta pCO_2}$ is the fractional uncertainty in the difference between $pCO_{2(sw)}$ and $pCO_{2(air)}$. Substituting values from above, we obtain:

$$\partial F_{CO_2} = F_{CO_2}\sqrt{(0.2)^2 + (0.04)^2 + \frac{(6)^2 + (31.7)^2}{(pCO_{2(sw)} - pCO_{2(air)})^2}}. \quad (3)$$

The mean and standard deviation of uncertainty estimates for different flux values (Fig. 8) ranged from 1.9 ± 1.0 mmol C m^{-2} d^{-1} at low fluxes ($|F_{CO_2}| \leq 2.0$) to 21.2 ± 2.8 mmol C m^{-2} d^{-1} at high negative fluxes ($F_{CO_2} \simeq -80$ mmol C m^{-2} d^{-1}) or 12.2 ± 6.0 mmol C m^{-2} d^{-1} at high positive fluxes ($F_{CO_2} \simeq 40$ mmol C m^{-2} d^{-1}). Expressed as percent error, mean uncertainties were > 100% for flux absolute values of < 2.0 mmol C m^{-2} d^{-1} and decreased to < 50% for flux absolute values exceeding 10 mmol C m^{-2} d^{-1}. These uncertainties, while relatively high for low fluxes, were comparable to or less than the spatial variability encountered in the different regions, as shown by the standard deviation ranges for the time-series of air-sea CO_2 fluxes in Fig. 7. For comparison, flux uncertainties reported by Huang et al. (2015a) for in situ data ranged from ± 0.05 to ± 2.98 mmol C m^{-2} d^{-1} (overall mean of 1.15 mmol C m^{-2} d^{-1}).

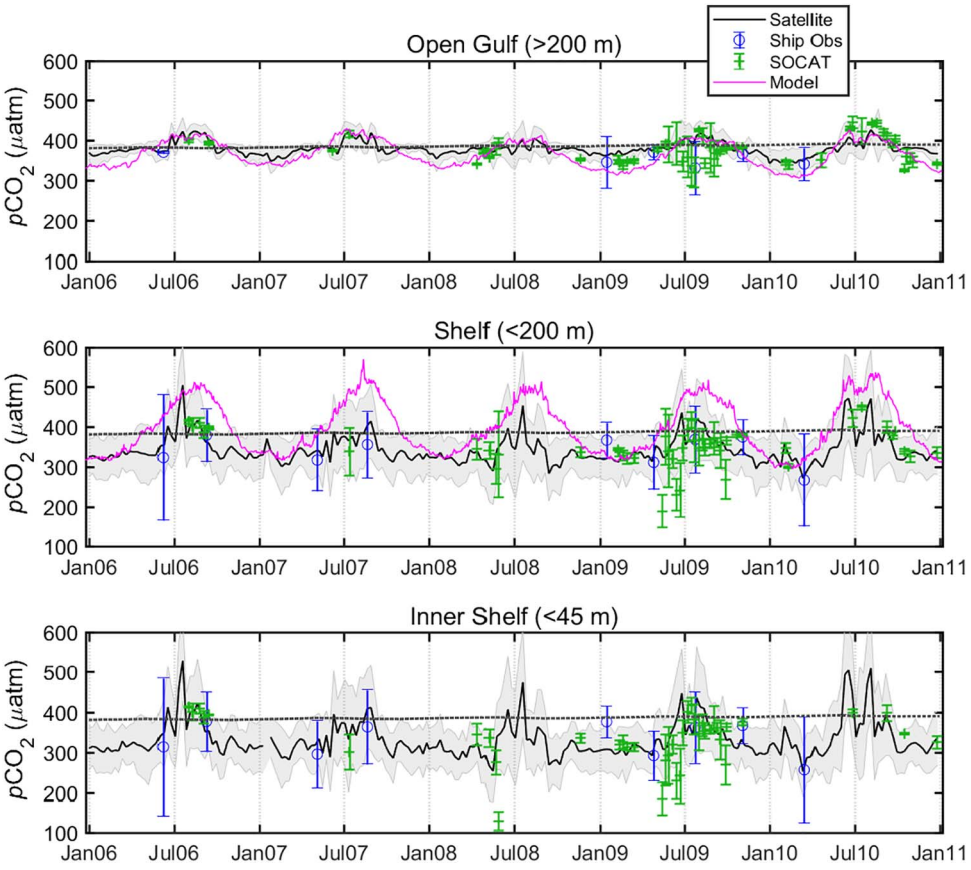

Fig. 6. Time-series of surface water pCO_2 derived from a satellite algorithm (solid black line) trained using ship-based observations (blue open symbols) and compared to independent observations for the same region from the SOCAT database (green symbols), and to the SABGOM-ROMS model (magenta line). Shaded areas are plus or minus one standard deviation around the mean satellite-derived pCO_2. Symbol error bars also represent plus or minus one standard deviation around the mean. The dashed line represents the atmospheric pCO_2.

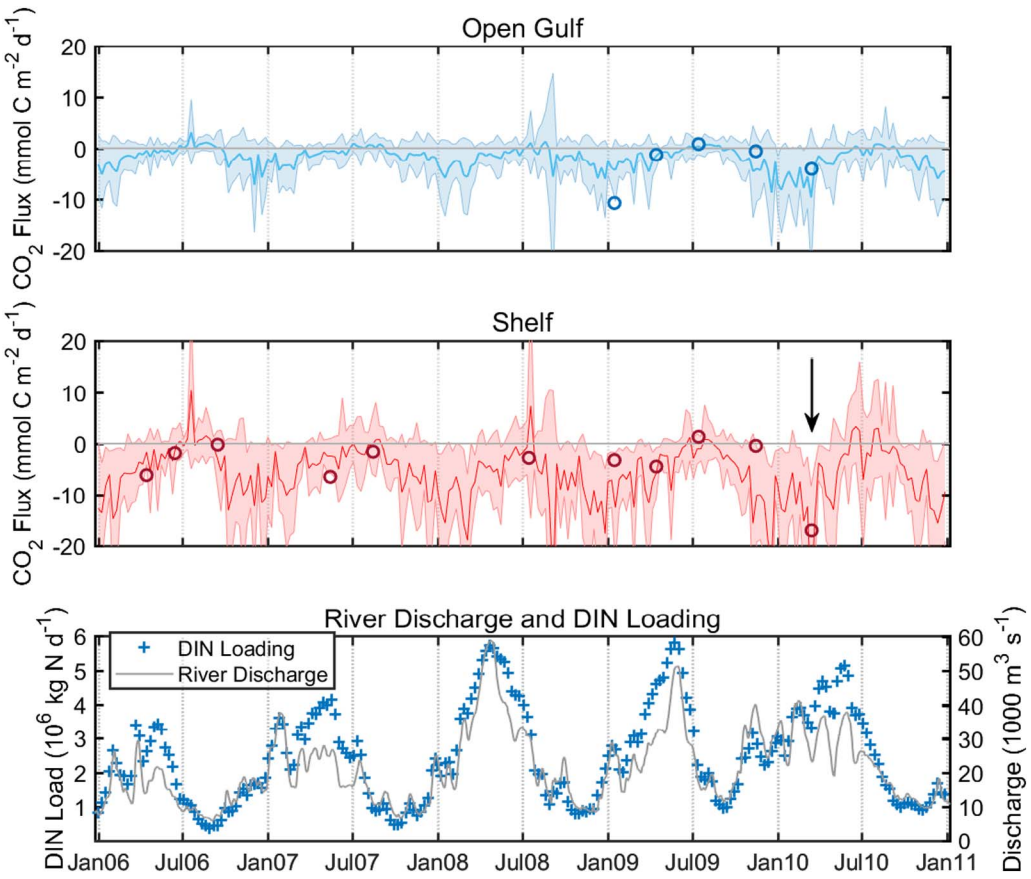

Fig. 7. Estimates of sea-to-air flux of CO_2 were made using the satellite-derived estimates of pCO_2 and using the wind parameterization of Wanninkhof (2014). The shaded areas in the top two panels represent plus or minus one standard deviation around the mean. The circle symbols are results from Huang et al. (2015a, 2015b) for comparison (shelf values shown are the mean of their inner, middle and outer shelf estimates). The vertical black arrow indicates the period of strong uptake of CO_2 during March 2010. Combined river discharge and dissolved inorganic nitrogen (DIN) loading from the Mississippi and Atchafalaya rivers are provided in the bottom panel for comparison. Nutrient data were provided courtesy of United States Geological Survey from the St. Francisville (water quality station number 07373420) and Melville (water quality station number 07381495) NASQAN sites. DIN loading was estimated from the combination of nutrient concentrations and river discharge as described in Lohrenz et al. (2013).

Table 4
Mean (± standard deviation) of monthly estimates of air-sea flux of CO_2 (mmol C m^{-2} d^{-1}).

Month	Open gulf	Shelf	Inner shelf	Outer shelf	Total
1	− 4.1 ± 1.8	− 9.4 ± 3.5	− 10.8 ± 4.2	− 7.4 ± 2.7	− 5.6 ± 2.2
2	− 3.9 ± 1.8	− 9.3 ± 3.4	− 10.7 ± 4.1	− 7.1 ± 2.8	− 5.6 ± 2.2
3	− 2.7 ± 2.3	− 8.0 ± 7.0	− 9.4 ± 7.6	− 5.9 ± 6.0	− 4.3 ± 3.7
4	− 1.6 ± 0.8	− 5.1 ± 2.5	− 6.4 ± 3.0	− 3.3 ± 1.9	− 2.7 ± 1.2
5	− 1.0 ± 0.7	− 3.9 ± 3.1	− 5.1 ± 3.9	− 2.4 ± 1.8	− 1.9 ± 1.5
6	− 0.4 ± 0.6	− 0.9 ± 2.2	− 1.0 ± 2.8	− 0.8 ± 1.2	− 0.6 ± 1.1
7	0.2 ± 1.0	− 0.2 ± 3.7	− 0.5 ± 4.7	0.0 ± 2.1	0.1 ± 1.8
8	0.5 ± 0.6	− 1.1 ± 3.2	− 1.7 ± 3.9	− 0.2 ± 2.2	0.0 ± 1.3
9	− 0.9 ± 1.4	− 4.5 ± 5.8	− 5.5 ± 6.7	− 2.9 ± 4.0	− 2.2 ± 3.2
10	− 2.1 ± 0.8	− 7.4 ± 2.7	− 9.2 ± 3.6	− 4.7 ± 1.6	− 3.7 ± 1.4
11	− 2.5 ± 1.3	− 8.7 ± 3.3	− 10.5 ± 3.9	− 5.7 ± 2.6	− 4.5 ± 1.9
12	− 4.0 ± 2.2	− 11.6 ± 4.8	− 13.6 ± 5.6	− 8.3 ± 3.7	− 6.4 ± 2.9

Table 5
Cross-correlation of Mississippi-Atchafalaya river system DIN loading and discharge with satellite-derived chlorophyll, adg443, sst, pCO_2 and CO_2 flux. Lags indicate the shift in timing of DIN loading or river discharge relative to the satellite-derived products corresponding to the maximum correlation.

Variable 1	Variable 2	Region	*r*	*p*	Lag (days)
DIN flux	chlor_a	Open Gulf	0.347	$p \ll 0.001$	112
DIN flux	chlor_a	Shelf	0.355	$p \ll 0.001$	8
DIN flux	chlor_a	Inner Shelf	0.482	$p \ll 0.001$	0
DIN flux	adg_443_gsm	Open Gulf	0.428	$p \ll 0.001$	24
DIN flux	adg_443_gsm	Shelf	0.418	$p \ll 0.001$	0
DIN flux	adg_443_gsm	Inner Shelf	0.466	$p \ll 0.001$	0
DIN flux	sat_sst	Open Gulf	0.676	$p \ll 0.001$	112
DIN flux	sat_sst	Shelf	0.693	$p \ll 0.001$	96
DIN flux	sat_sst	Inner Shelf	0.701	$p \ll 0.001$	96
DIN flux	pCO_2	Open Gulf	0.534	$p \ll 0.001$	112
DIN flux	pCO_2	Shelf	0.495	$p \ll 0.001$	80
DIN flux	pCO_2	Inner Shelf	0.501	$p \ll 0.001$	72
DIN flux	CO_2 flux	Open Gulf	0.501	$p \ll 0.001$	104
DIN flux	CO_2 flux	Shelf	0.447	$p \ll 0.001$	88
DIN flux	CO_2 flux	Inner Shelf	0.450	$p \ll 0.001$	80
Discharge	chlor_a	Open Gulf	0.207	0.002	0
Discharge	chlor_a	Shelf	0.439	$p \ll 0.001$	24
Discharge	chlor_a	Inner Shelf	0.542	$p \ll 0.001$	16
Discharge	adg_443_gsm	Open Gulf	0.493	$p \ll 0.001$	24
Discharge	adg_443_gsm	Shelf	0.485	$p \ll 0.001$	0
Discharge	adg_443_gsm	Inner Shelf	0.540	$p \ll 0.001$	0
Discharge	sat_sst	Open Gulf	0.445	$p \ll 0.001$	120
Discharge	sat_sst	Shelf	0.468	$p \ll 0.001$	112
Discharge	sat_sst	Inner Shelf	0.475	$p \ll 0.001$	112
Discharge	pCO_2	Open Gulf	0.324	$p \ll 0.001$	120
Discharge	pCO_2	Shelf	0.310	$p \ll 0.001$	112
Discharge	pCO_2	Inner Shelf	0.337	$p \ll 0.001$	72
Discharge	CO_2 flux	Open Gulf	0.311	$p < 0.001$	104
Discharge	CO_2 flux	Shelf	0.281	$p \ll 0.001$	104
Discharge	CO_2 flux	Inner Shelf	0.288	$p \ll 0.001$	88

4. Discussion

4.1. Satellite estimation of pCO_2 and air-sea flux of CO_2

Satellite approaches to estimate pCO_2 and air-sea flux of CO_2 have been increasingly used and provide a considerable advantage over exclusively ship-based or buoy observations in enabling extrapolation over wider spatial and temporal scales. The present study provides an illustration of the utility of satellite-derived time-series in both pCO_2 and air-sea flux of CO_2 for delineating patterns in relationship to seasonal forcing and other environmental drivers such as river discharge. The results also provide examples of how satellite time-series enable the elucidation of episodic and spatially-localized events, which can be difficult to detect or fully characterize with ship-based observations. While a number of other studies have applied satellite algorithms for estimation of pCO_2 and air-sea flux of CO_2 in coastal margins (Bai et al., 2015; Chen et al., 2016; Hales et al., 2012; Lohrenz and Cai, 2006; Lohrenz et al., 2010; Nakaoka et al., 2013; Signorini et al., 2013; Zhu et al., 2009), this is the first such assessment over a multi-year period for the northern Gulf of Mexico. Chen et al. (2016) used a multiple nonlinear regression approach to derive estimates of pCO_2 from satellite observations of chlorophyll, diffuse attenuation, and SST on the west Florida Shelf. They obtained an RMSE of ~11 µatm. In addition to their analysis of the west Florida Shelf region, they conducted a preliminary analysis of surface pCO_2 in the northern Gulf of Mexico using their multivariate approach, although they did not estimate air-sea flux of CO_2. They obtained a slightly larger RMSE (44.1 µatm as compared to our PE of 31.7 µatm and RMSE of 28.8 µatm). Signorini et al. (2013) used a combination of multiple linear regression and spatial binning to develop satellite estimates of pCO_2 for different regions on the eastern U.S. continental shelf. Values of RMSE ranged from 22.4–36.9 µatm pCO_2. A combination of self-organizing maps and a nonlinear semi-empirical model was used to derive estimates of pCO_2 on the North American west coast (Hales et al., 2012), which yielded a numerically averaged RMSE for all regions of 57.8 µatm and an area-weighted average of 24.5 µatm. We contend that the regression tree algorithm used in this present study performed well – comparable to or better than other methods, even in the highly complex and heterogeneous northern Gulf of Mexico region. We acknowledge that the complex optical environment in river-influenced northern Gulf of Mexico poses a challenge for the application of satellite algorithms. We found that the satellite-derived products for the selected variables (chlor_a, adg_443_gsm, sat_sst) were generally representative of in situ observations (Fig. S1), but also note that future work should explore the potential for improved performance of the pCO_2 algorithm using other satellite-derived indices (e.g., Kd_531_lee). An additional topic for further study is a consideration of the sensitivity of the algorithm to spatial

Table 6
Mean (± standard deviation) of annual estimates of air-sea flux of CO_2 (mol C m^{-2} y^{-1}) and DIN loading (Tg N y^{-1}).

Year	Open gulf	Shelf	Inner shelf	Outer shelf	Total	DIN loading
2006	− 0.5 ± 0.7	− 1.8 ± 1.9	− 2.2 ± 2.3	− 1.1 ± 1.3	− 0.9 + 1.1	0.6 + 0.3
2007	− 0.4 ± 0.5	− 1.5 ± 1.2	− 1.9 ± 1.4	− 1.0 ± 0.9	− 0.8 + 0.7	0.8 + 0.4
2008	− 0.8 ± 0.7	− 2.7 ± 2.2	− 3.3 ± 2.5	− 1.9 ± 1.6	− 1.4 + 1.2	1.0 + 0.6
2009	− 0.7 ± 0.7	− 2.1 ± 1.9	− 2.5 ± 2.2	− 1.4 ± 1.4	− 1.1 + 1.1	1.1 + 0.5
2010	− 1.0 ± 1.0	− 2.5 ± 2.4	− 2.9 ± 2.7	− 2.0 ± 1.9	− 1.5 + 1.4	1.0 + 0.5

Table 7
Mean (± standard deviation) of annual CO_2 fluxes for the different subregions within the study area in (Tg C y^{-1}).

Year	Open gulf	Shelf	Inner shelf	Outer shelf	Total
2006	− 1.2 ± 1.6	− 2.3 ± 2.5	− 2.0 ± 2.0	− 0.5 ± 0.5	− 3.5 ± 3.0
2007	− 1.0 ± 1.0	− 2.0 ± 1.6	− 1.7 ± 1.3	− 0.4 ± 0.4	− 3.0 ± 1.9
2008	− 1.8 ± 1.6	− 3.6 ± 2.9	− 3.0 ± 2.3	− 0.8 ± 0.7	− 5.4 ± 3.3
2009	− 1.4 ± 1.6	− 2.7 ± 2.5	− 2.2 ± 2.0	− 0.6 ± 0.6	− 4.2 ± 3.0
2010	− 2.3 ± 2.2	− 3.4 ± 3.1	− 2.6 ± 2.4	− 0.8 ± 0.8	− 5.6 ± 3.8
Overall mean	− 1.5 ± 0.5	− 2.8 ± 0.7	− 2.3 ± 0.5	− 0.6 ± 0.2	− 4.3 ± 1.1

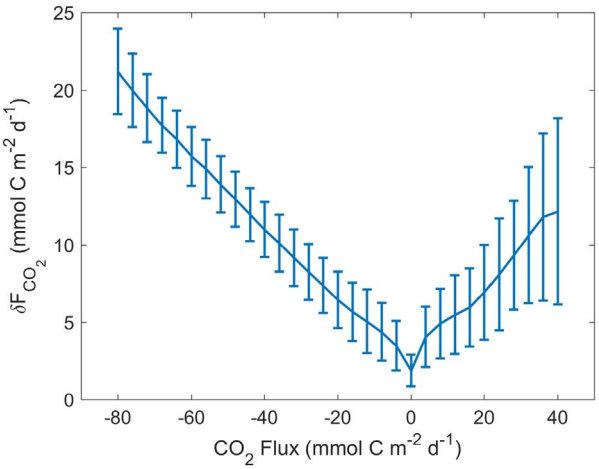

Fig. 8. Mean and standard deviations of uncertainty for 8-day composite air-sea CO_2 flux estimates for the time period 2006–2010.

resolution in satellite products used to train the algorithm. As noted previously, we found that the algorithm trained using the 1.1 km resolution data did not perform as well in representing the full extent of temporal variability observed in pCO_2 (cf. Fig. 6 and Fig. S9). We speculate that this was due to an effective reduction in the number of satellite matchups with ship-based observations for the reduced resolution training dataset. This limited the possible model outcomes for given combinations of environmental variables and consequently tended to dampen the range of variability in the model-simulated results.

Our findings of temporal and spatial variability in air-sea CO_2 fluxes were consistent with those of prior studies based on shipboard observations (Huang et al., 2015a) and support the view that the Gulf of Mexico, specifically the region encompassing the river-influenced northern Gulf of Mexico, is a net sink for atmospheric CO_2. Our estimates of annual per unit area CO_2 fluxes ranged from − 0.8 to − 1.5 (annual mean = − 1.1 ± 0.3) mol C m^{-2} y^{-1} (Table 6), where the negative sign indicates ocean uptake. This was consistent with the per unit area CO_2 flux of − 0.96 ± 3.7 mol C m^{-2} y^{-1} given by Huang et al. (2015a). We derived a much higher total annual CO_2 flux for our study region of − 4.3 ± 1.1 Tg C y^{-1}, compared to an estimate of − 1.2 ± 4.4 Tg C y^{-1} reported by Huang et al. (2015a). However, their value was based on a much smaller area. Using their area estimate (74.8×10^3 km^2) along with our mean annual per unit area CO_2 flux, we obtained an average annual air-to-sea CO_2 flux of − 1.0 ± 0.3 Tg C y^{-1}, similar to the Huang et al. (2015a) value. This net ocean uptake of carbon in the region is notable in light of the large fluvial input of ~17 Tg C y^{-1} bicarbonate carbon (Huang et al., 2015a) and 8.6 Tg C y^{-1} total organic carbon (Lohrenz et al., 2013).

Our assessment of the northern Gulf of Mexico air-sea CO_2 fluxes can be compared to findings of other studies that have estimated air-sea flux of CO_2 using satellite-based approaches. Satellite-derived estimates for the eastern continental U.S. region varied from − 2.12 Tg C y^{-1} in the Mid-Atlantic Bight to near zero fluxes of 0.007 Tg C y^{-1} for the Scotian Shelf (Signorini et al., 2013). Hales et al. (2012) estimated a much higher ocean uptake of CO_2 on the North American west coast of approximately 14 Tg C y^{-1}, largely attributable to strong upwelling in that region.

An examination of the pattern of pCO_2 distributions along the salinity gradient (Fig. 5) provided insight as to underlying factors controlling spatial patterns. A downward curvilinear shape in the pCO_2-salinity relationship was observed, with lower values at intermediate salinities and higher values at low salinities corresponding to high fluvial inputs of dissolved inorganic carbon and total alkalinity, and at the highest salinities corresponding to the high temperature and low production open ocean conditions (Guo et al., 2012; Huang et al., 2015a). The low values of pCO_2 at intermediate salinities can be explained by a strong biological drawdown of CO_2 associated with the high productivity (Guo et al., 2012; Lohrenz et al., 1999; Lohrenz et al., 2008), particularly during spring and summer months. While trends in satellite-derived and ship-based estimates of pCO_2 along the salinity gradient were generally comparable, there were some differences, such as at low salinities during May 2007. The region around the delta is especially dynamic and spatially heterogeneous (Figs. S5–7) and, therefore, differences can be expected between ship-based point measurements and satellite observations, especially in the mid- and low salinity regions. For example, sharp spatial gradients (Huang et al., 2015a) could lead to intrapixel variability that may have contributed to observed differences. Differences between satellite-derived and ship-based estimates of pCO_2 were also noted at high salinities in the case of September 2006 and July 2009 (Fig. 5). These were likely due to a limited number of satellite matchups with ship-based observations in the offshore waters, such that the algorithm did not adequately capture the full range of environmental variability. These examples highlight the challenges of matching point observations to satellite-observed signals in a highly dynamic and heterogeneous coastal region. Despite this, the overall trends in the satellite estimates were consistent with the ship-based data.

Regions of reduced surface pCO_2 were evident in the vicinity of the river and inner shelf regions in the pCO_2 imagery (Fig. 4), and high values of chlor_a in the shelf region (Fig. S5) was consistent with a strong biological influence. Offshore distributions of pCO_2 were characterized by distinct features in some of the imagery and we speculate that these may have been, in some cases, influenced by major circulation phenomena such as the Loop Current and its associated eddies and meanders (Oey et al., 2005). A Loop Current feature could be seen, for example, in January 2009 and March 2010 composite sat_sst images (Fig. S7). Offshore extensions of low pCO_2 features were present in some images, for example in July 2009 and March 2010. We acknowledge that data density for in situ measurements of pCO_2 was relatively low in the deep offshore waters of the Gulf of Mexico (see Fig. 1 for coverage); algorithm performance could be improved with increased spatial and temporal resolution of in situ training data. Huang et al. (2015a) provided a conceptual model of the pattern of air-sea exchange of CO_2 along the salinity gradient consistent with our findings. Their model is a representation of a river-influenced source of CO_2 in the inner shelf at low salinities which transitions to a region of high productivity and drawdown of CO_2 at mid-salinities, while offshore waters shift towards near neutral status.

4.2. Seasonal variations in pCO_2 and air-sea flux of CO_2

Seasonal variability evident in time-series of pCO_2 (Fig. 6) and air-sea fluxes of CO_2 (Fig. 7, Table 4) reflected a combination of variations in environmental conditions and associated biological effects, likely to some extent mediated by river inputs. A similar seasonal pattern was reported by Huang et al. (2015a), based on shipboard observations compiled over multiple years. The observed pattern of seasonal variability was also consistent with that of a coupled physical-biogeochemical model (Xue et al., 2016), results of which are compared in Fig. 6.

The significant relationships of DIN loading and river discharge with satellite-derived chlor_a, adg_443, pCO_2, and air-sea flux of CO_2 (Table 5) provided evidence for a significant influence of the river on the biogeochemistry of the region. Prior studies have demonstrated a relationship between satellite-derived chlorophyll and river DIN loading in the vicinity of the river plume (Lohrenz et al., 2013; Lohrenz et al., 2008), which was consistent with our findings. Similarly, there is a well-documented relationship between river discharge and colored dissolved organic matter absorption (related to adg_443) (Del Castillo and Miller, 2008; Green et al., 2008). The findings of these prior studies along with the positive correlations with relatively short lags reported here for chlor_a and adg_443 (Table 5), can be explained by enhanced biological activity related to nutrient inputs as well as high inputs of dissolved and detrital organic matter from the river. In contrast to the short lag observed for shelf and inner shelf chlor_a, there was a long lag between DIN loading and open Gulf chlor_a of 112 d (Table 5). The longer lag might be explained by a time delay due to the period of transit of river water from the point of upriver measurements to Gulf waters. This was in contrast to a zero lag between river discharge and open Gulf chlor_a. The correlation between river discharge and open Gulf chlor_a was quite low, and likely does not reflect a direct relationship.

We also observed positive correlations of DIN loading and river discharge with pCO_2 and CO_2 flux, but with a long lag of 72 to 104 days. This similarly raised the question of whether there was a direct causal linkage between the river inputs and the higher and more variable values of pCO_2 and more positive CO_2 flux for shelf waters in summer months. The higher pCO_2 and more positive air-sea flux of CO_2 could in part be related to decomposition of organic matter, either terrestrial organic matter supplied by the river or autochthonous organic matter produced by nutrient-enhanced primary production. It is also reasonable to surmise that the higher summer temperatures could reinforce such a seasonal pattern, the higher temperatures both accelerating decomposition and reducing the solubility of CO_2 in surface waters. Xue et al. (2016) reported a negative correlation between pCO_2 and surface salinity and positive correlation of pCO_2 with DIN in shelf waters and suggested that high turbidity of river waters may have constrained rates of primary production and that combined with the high inorganic carbon content of the river could have resulted in increased levels of pCO_2 and positive CO_2 flux. Justic et al. (1993) reported a two month lag between river flow and bottom water hypoxia at a site to the west of the Mississippi River delta, and attributed this to coupling between river nutrients, net productivity and delivery of organic matter and its decomposition in bottom waters. We acknowledge that a causal relationship between river DIN loading and discharge with other variables can only be inferred from correlations. For example, patterns of temporal variation, particularly for open Gulf waters, may simply reflect a seasonal signal that is not necessarily directly linked to river inputs. The seasonal variation in temperature could explain the longer lags in sat_sst (96 to 120 days) relative to river DIN loading and discharge (Table 5), and these lags were similar to that observed for pCO_2 and CO_2 flux.

4.3. Environmental forcing and inter-annual variations pCO_2 and air-sea CO_2 fluxes

Satellite extrapolations of pCO_2 allow the examination of the influence of environmental factors such as the combination of river discharge, wind forcing and mesoscale circulation phenomena. The period of March 2010 corresponded to an extensive area of low pCO_2 in shelf waters (Fig. 4) and strong ocean uptake of CO_2 (Fig. 7). This period was also associated with anomalously high chlorophyll concentrations (Fig. S5), low sea surface temperatures (Fig. S7), and strong offshore wind forcing (Huang et al., 2013). The pattern of river discharge and DIN loading was also unusually high during the period leading up to March 2010 (Fig. 7, bottom panel). These conditions resulted in a widespread plume event that was associated with low pCO_2 (Huang et al., 2013). In a separate study, Huang et al. (2015b) examined the period of July 2009, during which strong upwelling favorable winds resulted in an offshore distribution of river influenced low pCO_2 water. This was contrasted with conditions during August 2007 more representative of average climatology in which the plume is confined to the inner shelf. Patterns evident in our monthly composite images of pCO_2 for Aug 2007 and Jul 2009 (Fig. 4) were consistent with their findings, in that a region of relatively low pCO_2 could be seen extending well off the delta region into offshore waters in July 2009 as compared to August 2007. Higher values of chlor_a were also evident in offshore waters during July 2009 as compared to August 2007 (Fig. S5). Other studies have documented through satellite observations and modeling the interactions of the Mississippi River plume with wind forcing, topography, and shelf-slope circulation (Schiller et al., 2011; Walker et al., 2005). Our results provide further evidence of the spatially extensive influence of the river as modified by environmental forcing, and potential impacts on regional carbon cycling and air-sea exchange.

Interannual variations were evident in air-sea flux of CO_2 with more negative values during the latter years of the study, and this coincided with higher levels of river DIN loading (Tables 6 and S3). Thus, in contrast to the lagged positive correlations of CO_2 flux with discharge and DIN loading on a seasonal basis (Table 5), more negative mean annual CO_2 fluxes on a regional basis were associated with higher DIN loading (Tables 6, S3 and S4). This finding is consistent with that of prior studies highlighting relationships between river inputs and regional primary production or net community production (Justic et al., 1993; Lohrenz et al., 1997, 1999, 2008; Xue et al., 2016). These results demonstrate a need for further study to resolve the linkages between the extent and temporal variability of river inputs and both seasonal and annual scale carbon dynamics in this region.

5. Conclusions

The present study provides the first multi-year assessment of pCO_2 and air-sea flux of CO_2 using satellite-derived environmental data for the northern Gulf of Mexico, and illustrates the utility of satellite approaches as a complement to ship-based and buoy observations, allowing coverage over more extended spatial and temporal scales. The regression tree algorithm used here performed well for the region studied, and should be readily applicable to other regions for which there are adequate in situ pCO_2 observations and other supporting satellite-derived environmental data. As the availability of in situ data increases, it is expected that the satellite method described here would be able to improve in performance. The combined approach of a quality in situ data set complemented by synoptic satellite coverage may also lead to improved precision of estimates of carbon exchanges by accounting for temporal and spatial patterns not accessible through in situ observations alone. For example, the satellite observations can provide temporal and spatial continuity over time scales beyond that of ship- and buoy-based measurements and can capture effects of episodic environmental forcing on carbon processes. While it is acknowledged that applications of the satellite-derived algorithm beyond the time and

space domain of the training data set must be interpreted critically, the satellite approach is nonetheless useful in highlighting features and regions which may contribute significantly to carbon signals and for which more observations should be prioritized. Coupled with other approaches such as semi-mechanistic algorithms (Bai et al., 2015; Hales et al., 2012) or coupled physical-biogeochemical models (Xue et al., 2016), it should be possible to considerably advance our ability to quantify spatial and temporal variations in carbon fluxes and underlying drivers of those variations. Our results add to a growing body of evidence that in the context of a rapidly changing global environment, natural and anthropogenic changes in movement of water, carbon and nutrients through terrestrial systems have the potential to dramatically alter carbon processes in coastal and adjacent ocean environments (Borges, 2011), particularly in the case of large river-dominated margin ecosystems.

Acknowledgements

Research support was provided through the National Aeronautics and Space Administration (NNX10AU06G, NNX12AP84G, NNX14AO73G); National Science Foundation (OCE-0752254 and OCE-0752110); and NOAA Grant NA11NOS0120033. We are grateful to the NASA Ocean Biology Processing Group for providing access to satellite data and processing tools. The Surface Ocean CO_2 Atlas (SOCAT) is an international effort, endorsed by the International Ocean Carbon Coordination Project (IOCCP), the Surface Ocean Lower Atmosphere Study (SOLAS) and the Integrated Marine Biosphere Research (IMBeR) program, to deliver a uniformly quality-controlled surface ocean CO_2 database. The many researchers and funding agencies responsible for the collection of data and quality control are thanked for their contributions to SOCAT. We also thank anonymous reviewers for very helpful feedback in the review process.

Appendix A. Supplementary data

Supplementary data to this article can be found online at https://doi.org/10.1016/j.rse.2017.12.039.

References

Atlas, R., Hoffman, R.N., Ardizzone, J., Leidner, S.M., Jusem, J.C., Smith, D.K., Gombos, D., 2011. A cross-calibrated, multiplatform ocean surface wind velocity product for meteorological and oceanographic applications. Bull. Am. Meteorol. Soc. 92, 157.

Bai, Y., Cai, W.J., He, X., Zhai, W., Pan, D., Dai, M., Yu, P., 2015. A mechanistic semi-analytical method for remotely sensing sea surface pCO_2 in river-dominated coastal oceans: a case study from the East China Sea. J. Geophys. Res. Oceans 120, 2331–2349.

Baith, K., Lindsay, R., Fu, G., McClain, C.R., 2001. Data analysis system developed for ocean color satellite sensors. EOS Trans. Am. Geophys. Union 82, 202.

Bakker, D.C.E., Pfeil, B., Landa, C.S., Metzl, N., O'Brien, K.M., Olsen, A., Smith, K., Cosca, C., Harasawa, S., Jones, S.D., Nakaoka, S.I., Nojiri, Y., Schuster, U., Steinhoff, T., Sweeney, C., Takahashi, T., Tilbrook, B., Wada, C., Wanninkhof, R., Alin, S.R., Balestrini, C.F., Barbero, L., Bates, N.R., Bianchi, A.A., Bonou, F., Boutin, J., Bozec, Y., Burger, E.F., Cai, W.J., Castle, R.D., Chen, L., Chierici, M., Currie, K., Evans, W., Featherstone, C., Feely, R.A., Fransson, A., Goyet, C., Greenwood, N., Gregor, L., Hankin, S., Hardman-Mountford, N.J., Harlay, J., Hauck, J., Hoppema, M., Humphreys, M.P., Hunt, C.W., Huss, B., Ibánhez, J.S.P., Johannessen, T., Keeling, R., Kitidis, V., Körtzinger, A., Kozyr, A., Krasakopoulou, E., Kuwata, A., Landschützer, P., Lauvset, S.K., Lefèvre, N., Lo Monaco, C., Manke, A., Mathis, J.T., Merlivat, L., Millero, F.J., Monteiro, P.M.S., Munro, D.R., Murata, A., Newberger, T., Omar, A.M., Ono, T., Paterson, K., Pearce, D., Pierrot, D., Robbins, L.L., Saito, S., Salisbury, J., Schlitzer, R., Schneider, B., Schweitzer, R., Sieger, R., Skjelvan, I., Sullivan, K.F., Sutherland, S.C., Sutton, A.J., Tadokoro, K., Telszewski, M., Tuma, M., van Heuven, S.M.A.C., Vandemark, D., Ward, B., Watson, A.J., Xu, S., 2016. A multi-decade record of high-quality fCO_2 data in version 3 of the Surface Ocean CO_2 Atlas (SOCAT). Earth Syst. Sci. Data 8, 383–413.

Bauer, J.E., Cai, W.J., Raymond, P.A., Bianchi, T.S., Hopkinson, C.S., Regnier, P.A.G., 2013. The changing carbon cycle of the coastal ocean. Nature 504, 61–70.

Behrenfeld, M.J., Westberry, T.K., Boss, E.S., O'Malley, R.T., Siegel, D.A., Wiggert, J.D., Franz, B.A., McClain, C.R., Feldman, G.C., Doney, S.C., Moore, J.K., Dall'Olmo, G., Milligan, A.J., Lima, I., Mahowald, N., 2009. Satellite-detected fluorescence reveals global physiology of ocean phytoplankton. Biogeosciences 6, 779–794.

Borges, A.V., 2011. Present day carbon dioxide fluxes in the coastal ocean and possible feedbacks under global change oceans and the atmospheric carbon content. In: Duarte, P., Santana-Casiano, J.M. (Eds.), Oceans and Atmospheric Carbon Content. Springer, Netherlands, pp. 47–77.

Borges, A.V., Delille, B., Frankignoulle, M., 2005. Budgeting sinks and sources of CO_2 in the coastal ocean: diversity of ecosystems counts. Geophys. Res. Lett. 32, L14601. http://dx.doi.org/10.11029/12005GL023053.

Cai, W.-J., 2003. Riverine inorganic carbon flux and rate of biological uptake in the Mississippi River plume. Geophys. Res. Lett. 30, 1032. http://dx.doi.org/10.1029/2002GL016312.

Cai, W.-J., 2011. Estuarine and coastal ocean carbon paradox: CO_2 sinks or sites of terrestrial carbon incineration? Annu. Rev. Mar. Sci. 3 (3), 123–145.

Cai, W.-J., Lohrenz, S.E., 2010. The Mississippi River plume and adjacent margin in the gulf of Mexico. In: Liu, K.-K., Atkinson, L., Quinoñes, R., Talaue-McManus, L. (Eds.), Carbon and Nutrient Fluxes in the Continental Margins: A Global Synthesis. Springer, Berlin, pp. 406–422.

Cai, W.J., Dai, M.H., Wang, Y.C., Zhai, W.D., Huang, T., Chen, S.T., Zhang, F., Chen, Z.Z., Wang, Z.H., 2004. The biogeochemistry of inorganic carbon and nutrients in the Pearl River estuary and the adjacent Northern South China Sea. Cont. Shelf Res. 24, 1301–1319.

Cai, W.-J., Dai, M.H., Wang, Y.C., 2006. Air-sea exchange of carbon dioxide in ocean margins: A province-based synthesis. Geophys. Res. Lett. 33, L12603. http://dx.doi.org/10.11029/12006GL026219.

Chen, C.T.A., Borges, A.V., 2009. Reconciling opposing views on carbon cycling in the coastal ocean: continental shelves as sinks and near-shore ecosystems as sources of atmospheric CO_2. Deep-Sea Res. II Top. Stud. Oceanogr. 56, 578–590.

Chen, S., Hu, C., Byrne, R.H., Robbins, L.L., Yang, B., 2016. Remote estimation of surface pCO_2 on the West Florida Shelf. Cont. Shelf Res. 128, 10–25.

Chierici, M., Signorini, S.R., Mattsdotter-Björk, M., Fransson, A., Olsen, A., 2012. Surface water fCO_2 algorithms for the high-latitude Pacific sector of the Southern Ocean. Remote Sens. Environ. 119, 184–196.

Cooley, S.R., Coles, V.J., Subramaniam, A., Yager, P.L., 2007. Seasonal variations in the Amazon plume-related atmospheric carbon sink. Glob. Biogeochem. Cycles 21, GB3014. http://dx.doi.org/10.1029/2006GB002831.

Dai, M., Chao, Z., Guo, X., Zhai, W., Liu, Z., Yin, Z., Xu, Y., Gan, J., Hu, J., Du, C., 2013. Why are some marginal seas sources of atmospheric CO2? Geophys. Res. Lett. 40. http://dx.doi.org/10.1002/grl.50390.

De'ath, G., Fabricius, K.E., 2000. Classification and regression trees: a powerful yet simple technique for ecological data analysis. Ecology 81, 3178–3192.

Del Castillo, C.E., Miller, R.L., 2008. On the use of ocean color remote sensing to measure the transport of dissolved organic carbon by the Mississippi River Plume. Remote Sens. Environ. 112, 836–844.

Dormann, C.F., Elith, J., Bacher, S., Buchmann, C., Carl, G., Carré, G., Marquéz, J.R.G., Gruber, B., Lafourcade, B., Leitão, P.J., 2013. Collinearity: a review of methods to deal with it and a simulation study evaluating their performance. Ecography 36, 27–46.

Goolsby, D.A., Battaglin, W.A., Lawrence, G.B., Artz, R.S., Aulenbach, B.T., Hooper, R.P., Keeney, D.R., Stensland, G.J., 1999. Flux and Sources of Nutrients in the Mississippi–Atchafalaya River Basin: Topic 3 Report for the Integrated Assessment on Hypoxia in the Gulf of Mexico. NOAA Decision Analysis Series U.S. Department of Commerce, NOAA Coastal Ocean Program, Silver Spring, MD.

Green, R.E., Gould, R.W., Ko, D.S., 2008. Statistical models for sediment/detritus and dissolved absorption coefficients in coastal waters of the northern Gulf of Mexico. Cont. Shelf Res. 28, 1273–1285.

Gruber, N., 2015. Ocean biogeochemistry: carbon at the coastal interface. Nature 517, 148–149.

Guo, X., Cai, W.-J., Zhai, W., Dai, M., Wang, Y., Chen, B., 2008. Seasonal variations in the inorganic carbon system in the Pearl River (Zhujiang) estuary. Cont. Shelf Res. 28, 1424–1434.

Guo, X., Dai, M., Zhai, W., Cai, W.-J., Chen, B., 2009. CO_2 flux and seasonal variability in a large subtropical estuarine system, the Pearl River Estuary, China. J. Geophys. Res. 114, G03013. http://dx.doi.org/10.01029/02008jg000905.

Guo, X., Cai, W.-J., Huang, W.-J., Wang, Y., Chen, F., Murrell, M.C., Lohrenz, S.E., Jiang, L.-Q., Dai, M., Hartmann, J., Lin, Q., Culp, R., 2012. Carbon dynamics and community production in the Mississippi River plume. Limnol. Oceanogr. 57, 1–17.

Hales, B., Strutton, P.G., Saraceno, M., Letelier, R., Takahashi, T., Feely, R., Sabine, C., Chavez, F., 2012. Satellite-based prediction of pCO_2 in coastal waters of the eastern North Pacific. Prog. Oceanogr. 103, 1–15.

Hu, C., Lee, Z., Franz, B., 2012. Chlorophyll aalgorithms for oligotrophic oceans: a novel approach based on three-band reflectance difference. J. Geophys. Res. Oceans 117 (C1). http://dx.doi.org/10.1029/2011JC007395.

Huang, W.-J., Cai, W.-J., Castelao, R.M., Wang, Y., Lohrenz, S.E., 2013. Effects of a wind-driven cross-shelf large river plume on biological production and CO_2 uptake on the Gulf of Mexico during spring. Limnol. Oceanogr. 58, 1727–1735.

Huang, W.-J., Cai, W.-J., Wang, Y., Lohrenz, S.E., Murrell, M.C., 2015a. The carbon dioxide system on the Mississippi River-dominated continental shelf in the northern Gulf of Mexico: 1. distribution and air-sea CO_2 flux. J. Geophys. Res. Oceans 120, 1429–1445.

Huang, W.-J., Cai, W.J., Wang, Y., Hu, X., Chen, B., Lohrenz, S.E., Chakraborty, S., He, R., Brandes, J., Hopkinson, C.S., 2015b. The response of inorganic carbon distributions and dynamics to upwelling-favorable winds on the northern Gulf of Mexico during summer. Cont. Shelf Res. 111 (Part B), 211–222.

Justic, D., Rabalais, N.N., Turner, R.E., Wiseman Jr., W.J., 1993. Seasonal coupling between riverborne nutrients, net productivity and hypoxia. Mar. Pollut. Bull. 26, 184–189.

Kortzinger, A., 2003. A significant CO_2 sink in the tropical Atlantic Ocean associated with the Amazon River plume. Geophys. Res. Lett. 30, 2287.

Laruelle, G.G., Dürr, H.H., Slomp, C.P., Borges, A.V., 2010. Evaluation of sinks and sources of CO_2 in the global coastal ocean using a spatially-explicit typology of estuaries and continental shelves. Geophys. Res. Lett. 37, L15607.

Laruelle, G.G., Lauerwald, R., Pfeil, B., Regnier, P., 2014. Regionalized global budget of the CO_2 exchange at the air-water interface in continental shelf seas. Glob. Biogeochem. Cycles 28, 1199–1214. http://dx.doi.org/10.1002/2014GB004832.

Laruelle, G.G., Lauerwald, R., Rotschi, J., Raymond, P., Hartmann, J., Regnier, P., 2015. Seasonal response of air-water CO_2 exchange along the land-ocean aquatic continuum of the northeast North American coast. Biogeosciences 12, 1447–1458.

Lee, Z.P., Carder, K.L., Arnone, R.A., 2002. Deriving inherent optical properties from water color: a multiband quasi-analytical algorithm for optically deep waters. Appl. Opt. 41, 5755–5772.

Lee, Z.-P., Du, K.-P., Arnone, R., 2005. A model for the diffuse attenuation coefficient of downwelling irradiance. J. Geophys. Res. Oceans 110. http://dx.doi.org/10.1029/2004JC002275.

Lefevre, N., Aiken, J., Rutllant, J., Daneri, G., Lavender, S., Smyth, T., 2002. Observations of pCO_2 in the coastal upwelling off Chile: spatial and temporal extrapolation using satellite data. J. Geophys. Res. Oceans 107, 3055. http://dx.doi.org/10.1029/2000JC000395.

Liu, K.-K., Atkinson, L., Quiñones, R.A., Talaue-McManus, L., 2010. Biogeochemistry of continental margins in a global context. In: Carbon and Nutrient Fluxes in Continental Margins. Springer, pp. 3–24.

Lohrenz, S.E., Cai, W.-J., 2006. Satellite ocean color assessment of air-sea fluxes of CO_2 in a river-dominated coastal margin. Geophys. Res. Lett. 33, L01601. http://dx.doi.org/10.01029/02005GL023942.

Lohrenz, S.E., Fahnenstiel, G.L., Redalje, D.G., Lang, G.A., Chen, X.G., Dagg, M.J., 1997. Variations in primary production of northern Gulf of Mexico continental shelf waters linked to nutrient inputs from the Mississippi River. Mar. Ecol. Prog. Ser. 155, 45–54.

Lohrenz, S.E., Fahnenstiel, G.L., Redalje, D.G., Lang, G.A., Dagg, M.J., Whitledge, T.E., Dortch, Q., 1999. Nutrients, irradiance, and mixing as factors regulating primary production in coastal waters impacted by the Mississippi River plume. Cont. Shelf Res. 19, 1113–1141.

Lohrenz, S.E., Redalje, D.G., Cai, W.-J., Acker, J., Dagg, M., 2008. A retrospective analysis of nutrients and phytoplankton productivity in the Mississippi River plume. Cont. Shelf Res. 28, 1466–1475.

Lohrenz, S.E., Cai, W.-J., Chen, F., Chen, X., Tuel, M., 2010. Seasonal variability in air-sea fluxes of CO_2 in a river-influenced coastal margin. J. Geophys. Res. 115, C10034.

Lohrenz, S.E., Cai, W.-J., Chakraborty, S., Gundersen, K., Murrell, M.C., 2013. Nutrient and carbon dynamics in a large river-dominated coastal ecosystem: the Mississippi-Atchafalaya River system. In: Bianchi, T.S., Allison, M.A., Cai, W.-J. (Eds.), Biogeochemical Dynamics at Major River-Coastal Interfaces: Linkages with Global Change. Cambridge University Press, pp. 448–472.

Maritorena, S., Siegel, D.A., Peterson, A.R., 2002. Optimization of a semianalytical ocean color model for global-scale applications. Appl. Opt. 41, 2705–2714.

Milliman, J.D., Meade, R.H., 1983. World-wide delivery of river sediment to the oceans. J. Geol. 91, 1–21.

Nakaoka, S., Telszewski, M., Nojiri, Y., Yasunaka, S., Miyazaki, C., Mukai, H., Usui, N., 2013. Estimating temporal and spatial variation of ocean surface pCO_2 in the North Pacific using a selforganizing map neural network technique. Biogeosciences 10, 6093–6106.

Oey, L.Y., Ezer, T., Lee, H.C., 2005. Loop current, rings and related circulation in the Gulf of Mexico: a review of numerical models and future challenges. In: Sturges, W., Lugo-Fernández, A. (Eds.), Circulation in the Gulf of Mexico: Observations and Models. American Geophysical Union, Washington, D.C., pp. 31–56.

Pierrot, D., Neill, C., Sullivan, K., Castle, R., Wanninkhof, R., Lüger, H., Johannessen, T., Olsen, A., Feely, R.A., Cosca, C.E., 2009. Recommendations for autonomous underway pCO_2 measuring systems and data-reduction routines. Deep-Sea Res. II Top. Stud. Oceanogr. 56, 512–522.

Reanalysis Data, N.C.E.P., 2017. NCEP Reanalysis-Derived Data Provided By the NOAA/OAR/ESRL PSD, Boulder, Colorado, USA. from their web site at. http://www.esrl.noaa.gov/psd/, Accessed date: 30 July 2017.

Ren, W., Tian, H., Tao, B., Yang, J., Pan, S., Cai, W.J., Lohrenz, S.E., He, R., Hopkinson, C.S., 2015. Large increase in dissolved inorganic carbon flux from the Mississippi River to Gulf of Mexico due to climatic and anthropogenic changes over the 21st century. J. Geophys. Res. Biogeosci. 120, 724–736.

Ren, W., Tian, H., Cai, W.-J., Lohrenz, S.E., Hopkinson, C.S., Huang, W.-J., Yang, J., Tao, B., Pan, S., He, R., 2016. Century-long increasing trend and variability of dissolved organic carbon export from the Mississippi River basin driven by natural and anthropogenic forcing. Glob. Biogeochem. Cycles 30, 1288–1299. http://dx.doi.org/10.1002/2016GB005395.

Robbins, L.L., Wanninkhof, R., Barbero, L., Hu, X., Mitra, S., Yvon-Lewis, S., Cai, W.-J., Huang, W.-J., Ryerson, T., 2014. Air-sea exchange. In: Benway, H.M., Coble, P.G. (Eds.), Report of the U.S, Gulf of Mexico Carbon Cycle Synthesis Workshop, March 27–28, 2013. Ocean Carbon and Biogeochemistry Program and North American Carbon Program, St. Petersburg, FL, pp. 17–23. http:/www.us-ocb.org/publications/GMx_report_FINAL.pdf.

Schiller, R.V., Kourafalou, V.H., Hogan, P., Walker, N.D., 2011. The dynamics of the Mississippi River plume: impact of topography, wind and offshore forcing on the fate of plume waters. J. Geophys. Res. 116, C06029.

Shadwick, E., Thomas, H., Comeau, A., Craig, S., Hunt, C., Salisbury, J., 2010. Air-Sea CO_2 fluxes on the Scotian Shelf: seasonal to multi-annual variability. Biogeosciences 7, 3851–3867.

Shim, J., Kim, D., Kang, Y.C., Lee, J.H., Jang, S.-T., Kim, C.-H., 2007. Seasonal variations in pCO_2 and its controlling factors in surface seawater of the northern East China Sea. Cont. Shelf Res. 27, 2623–2636.

Signorini, S.R., Mannino, A., Najjar, R.G., Friedrichs, M.A., Cai, W.J., Salisbury, J., Wang, Z.A., Thomas, H., Shadwick, E., 2013. Surface ocean pCO_2 seasonality and sea-air CO_2 flux estimates for the North American east coast. J. Geophys. Res. Oceans 118, 5439–5460.

Telszewski, M., Chazottes, A., Schuster, U., Watson, A.J., Moulin, C., Bakker, D.C.E., González-Dávila, M., Johannessen, T., Körtzinger, A., Lüger, H., Olsen, A., Omar, A., Padin, X.A., Ríos, A.F., Steinhoff, T., Santana-Casiano, M., Wallace, D.W.R., Wanninkhof, R., 2009. Estimating the monthly pCO_2 distribution in the North Atlantic using a self-organizing neural network. Biogeosciences 6, 1405–1421.

Ternon, J., Oudot, C., Dessier, A., Diverres, D., 2000. A seasonal tropical sink for atmospheric CO_2 in the Atlantic ocean: the role of the Amazon River discharge. Mar. Chem. 68, 183–201.

Tian, H., Ren, W., Yang, J., Tao, B., Cai, W.-J., Lohrenz, S.E., Hopkinson, C.S., Liu, M., Yang, Q., Lu, C., Zhang, B., Banger, K., Pan, S., He, R., Xue, Z., 2015. Climate extremes dominating seasonal and interannual variations in carbon export from the Mississippi River Basin. Glob. Biogeochem. Cycles 29, 1333–1347.

Tseng, C.-M., Shen, P.-Y., Liu, K.-K., 2014. Synthesis of observed air–sea CO_2 exchange fluxes in the river-dominated East China Sea and improved estimates of annual and seasonal net mean fluxes. Biogeosciences 11, 3855–3870.

Tsunogai, S., Watanabe, S., Sato, T., 1999. Is there a “continental shelf pump” for the absorption of atmospheric CO_2? Tellus B 51, 701–712.

Walker, N.D., Wiseman, W.J., Rouse, L.J., Babin, A., 2005. Effects of river discharge, wind stress, and slope eddies on circulation and the satellite-observed structure of the Mississippi River plume. J. Coast. Res. 21, 1228–1244.

Wanninkhof, R., 2014. Relationship between wind speed and gas exchange over the ocean revisited. Limnol. Oceanogr. Methods 12, 351–362.

Weiss, R.F., 1974. Carbon dioxide in water and seawater: the solubility of a non-ideal gas. Mar. Chem. 2, 203–215.

Weiss, R.F., Price, B.A., 1980. Nitrous oxide solubility in water and seawater. Mar. Chem. 8, 347–359.

Xue, Z., He, R., Fennel, K., Cai, W.J., Lohrenz, S., Huang, W.J., Tian, H., Ren, W., Zang, Z., 2016. Modeling pCO_2 variability in the Gulf of Mexico. Biogeosciences 13, 4359–4377.

Zhai, W., Dai, M., 2009. On the seasonal variation of air – sea CO_2 fluxes in the outer Changjiang (Yangtze River) Estuary, East China Sea. Mar. Chem. 117, 2–10.

Zhu, Y., Shang, S.L., Zhai, W.D., Dai, M.H., 2009. Satellite-derived surface water $pCO_{(2)}$ and air-sea CO_2 fluxes in the northern South China Sea in summer. Prog. Nat. Sci. 19, 775–779.